Complex spatial distribution of onset amplitude and waveform correlation: case studies from different DAS experiments

E. Bozzi[1], G. Saccorotti[2], N. Piana Agostinetti[1], C. Becerril[3], A. Fichtner[4], S. Klaasen[4], T. Nishimura[5], J. Shen[6], F. Walter[7], T. Zhu[6].

[1] University of Milano-Bicocca, Milano, Italy.

[2] Istituto Nazionale di Geofisica e Vulcanologia (INGV), Pisa, Italy.

[3] Université Côte d'Azur, CNRS, Observatoire de la Côte d'Azur, IRD, Géoazur, Valbonne, France

[4] ETH Zürich, Zürich, Switzerland

[5] Tohoku University, Tohoku, Japan

[6] PennState University, State College, Pennsylvania, USA

[7] Swiss Federal Institute for Forest, Snow and Landscape Research WSL, Uitikon, Switzerland

Key-words

Distributed Acoustic Sensing; seismic monitoring; azimuthal sensitivity; waveform correlation.

Abstract

Distributed Acoustic Sensing (DAS) technology repurposes fiber optic cables (FOCs) into seismic arrays, offering unprecedented dense strain/strain-rate measurements. The meter-scale virtual sensor spacing is typically unattainable with standard seismological equipment. Consequently, DAS provides an extraordinary amount of data suitable for seismic monitoring applications. However, peculiar features of this technology, such as signal axial polarization, coupling inhomogeneities or sensitivity to site conditions, can affect seismic phase amplitudes and their coherence, potentially reducing the number of useful measurement points. To gain a deeper understanding on the relative importance of these phenomena, this study analyzes *real data* from various seismic events recorded by shallow-horizontal DAS deployments. Thus, we take advantage of the pool of different array dimensions and geometries to avoid biased observations. We focus on the spatial variability of P-wave amplitudes, Signal-to-Noise Ratios (SNRs) and waveform correlation, ideally mimicking the usage of

absolute and differential arrival times for monitoring purposes. We observed significant amplitude variations which cannot be fully explained by signal polarization along the FOC. Additionally, waveform correlation often exhibits a complex and faster decay with interchannel distance. These findings suggest the importance of avoiding "blind" usage of shallow-horizontal DAS arrays and emphasize the need for case-dependent data selection/weighting procedures.

1 Introduction

DAS is a novel geophysical technology that allows for the re-purposing of FOCs into a dense array of seismic sensors (Zhan, 2020). DAS utilizes laser pulses from an interrogator at one of the FOC tips and detects phase changes in the back-scattered wavefield, following localized deformations of the FOC. This process maps very dense (meter scale) strain and strain rate measurements to each local position along the FOC (DAS channels), providing a detailed picture of e.g., a seismic wavefield (Cannon et al., 2013; Güemes et al., 2010; Mateeva et al., 2012; Mestayer et al., 2011; Parker et al., 2014). Therefore, DAS measures a physical quantity that is inherently different from that delivered by standard seismological instruments, such as ground acceleration, velocity, or displacement (Lindsey et al., 2020; Trabattoni et al., 2022). This characteristic makes the interrogated cable more sensitive to the elastic properties of the medium (Piana Agostinetti et al., 2022; Trabattoni et al., 2022,2023; Van den Ende and Ampuero, 2021). Additionally, the system only detects the strain component oriented along the FOC direction. This implies a selective sensitivity which, for a given wavetype, depends on the angle between the FOC orientation and the propagation azimuth and dip angles (Kennett et al., 2022; Martin et al., 2021; Trabattoni et al., 2022). Furthermore, the FOCs can be buried at different depths and characterized by peculiar noise sources, thereby exhibiting different sensing capabilities to elastic disturbances (Celli et al., 2023; Miller et al., 2018).

DAS can record a wide range of sources and it offers the advantage of being potentially deployable in challenging environments (Biagioli et al., 2024; Cheng et al., 2021; Fichtner et al., 2022; Jousset et al., 2022; Lior et al., 2022; Klaasen et al., 2021; Walter et al., 2020). Additionally, DAS can leverage FOCs already installed but not currently employed for telecommunications (referred to as *dark fibers*), removing the requirement for costly new excavations (Biondi et al., 2021). The dense spatial sampling provided by DAS, simply unattainable with standard seismological sensors, additionally offers the advantage of signal redundancy. Consequently, seismological techniques that exploit signal coherence and delay time information may be particularly well-suited for the DAS method (Biagioli et al., 2024; Klaasen et al., 2021; Porras et al., 2024; Van der Ende and Ampuero, 2021).

Numerous DAS experiments have been conducted in recent years, covering diverse contexts and for various purposes. Following pioneering industry tests in the early 2010s (Mestayer et al; 2011;

Molenaar et al., 2011) successive studies have demonstrated the capabilities of DAS for: mapping subsurface heterogeneity (Ajo-Franklin et al., 2019; Jousset et al., 2018; Lindsey et al., 2019; Lior et al., 2022; Yang et al., 2022; Yuan et al., 2020), upper crust structural studies (Biondi et al., 2023), monitoring natural (Lindsey et al., 2017; Ugalde et al., 2022) or induced seismicity (Karrenbach et al., 2019), particularly in geothermal fields (Lellouch et al., 2020; Obermann et al., 2022), enabling rapid response to study aftershock sequences (Li et al., 2021), characterizing natural seismicity resulting from glacier movements (Walter et al., 2020), and sensing urban noise (Biondi et al., 2021; Shen and Zhu, 2021). Nowadays, DAS is becoming increasingly used for standard seismological applications (Fernández-Ruiz et al., 2022; Li et al., 2023; Trabattoni et al., 2022; Wuestefeld et al., 2023).

In the traditional approach to earthquake detection and location, the amplitude of the signal's onset is crucial, particularly for arrival time picking methods that only rely on signal amplitudes such as the Short-Time / Long-Time-Average ratio (STA/LTA; Allen, 1982). Lower SNRs imply more uncertain measurements of arrival times, which in turn provoke larger errors in the estimate of the hypocentral parameters. Typically, the limited number of conventional seismic sensors, compared to DAS, allows for a manual inspection of the seismic waveforms to identify and exclude outliers originating from recordings with lower SNR. However, this procedure is operationally not feasible for DAS data, due to the presence of, typically, > 1000 channels in a single experiment.

In array seismology, different measures of signal coherence are used to extract information regarding Direction-Of-Arrival (DOA) and apparent propagation velocity of waves crossing the array (e.g., Rost and Thomas, 2002). Several authors have thus investigated the application of array techniques to DAS data (Van der Ende and Ampuero, 2021; Klaasen et al., 2021). However, local velocity heterogeneities and different cable orientations with respect to the DOA induce lateral variations of signal coherence, which restrict the applicability of multichannel techniques to the estimation of wavefield parameters (e.g., Van der Ende and Ampuero, 2021).

The above-mentioned considerations indicate that the performance of DAS systems in characterizing seismic sources at the local/regional scale is influenced by various factors, both intrinsic to the method (e.g., signal polarization) and installation-dependent (e.g., site effects, FOC coupling). While we have partial control over DAS geometrical features, such as cable orientation to the incident wavefield (Martin et al., 2021), our modelling capability is limited regarding site effects and coupling. This implies that we need an a-priori knowledge of the very local medium hosting the FOCs (Celli et al., 2023), and detailed knowledge about the cable setting.

This study aims to provide a deeper understanding of the influence of geometrical and site-dependent factors on the spatial variability of onset amplitudes and waveform correlation. Our "real-world" dataset is represented by recordings of 15 seismic events from as many DAS deployments, covering various installation environments and geometries (Fig. 1). Data acquired from wells are intentionally

excluded since we focus the analysis on the effects related to cable geometry (i.e., axial sensitivity related to azimuth variation) and the complex pool of surface-related issues. The dataset, covering DAS deployment installed between 2017 and 2021, includes a variety of recorded signals such as earthquakes, volcano-tectonic earthquakes, and ice quakes. For each DAS deployment, we select a seismic event with a known localization, in order to perform a first-order modeling of the geometrical factors. The first part of the study, following waveform pre-processing and onset picking, focuses on the spatial variations of onset amplitude. We analyze these variations against the expected axial sensitivity, also accounting for geometrical spreading and anelastic attenuation. Thus, our objective is to better understand the relative importance of 'predictable' factors (e.g., axial polarization of the signal and source-to-receiver distance) versus 'non-predictable' effects (i.e., coupling, unmodeled velocity heterogeneities) on the observed onset amplitudes. In the second part of the study, we examine signal correlation for selected cable portions and assess its decay with interchannel distance along with an expected trend. Indeed, while the first section primarily addresses potential issues related to the utilization of absolute arrival times, the second section is dedicated to applications which make use of differential arrival times.

2. Data and Methods

2.1. 15 “real-world” case studies

We analyze case studies derived from 15 DAS experiments conducted between 2017 and 2021 in diverse environments by different research groups. These datasets have been obtained either from open-access repositories (Feigl, 1969; Lindsey et al., 2020; Lior et al., 2021; Klaasen et al., 2021; Nishimura et al., 2021; Spica et al., 2023; Villasenor et al., 2020; Zhu et al., 2020) or restricted databases. The cable layouts and their geometrical relationships with the recorded events provide a substantial dataset for a comprehensive investigation of amplitude and coherency variations in DAS data. Three distinct installation environments have been defined to gather common case studies: 1) "submarine" telecommunication cables, 2) "terrestrial" telecommunication cables, and 3) "fit-for-purpose" installations. For each DAS array, recordings from well-located seismic events have been chosen, and hypocentral parameters have been obtained either from available seismic catalogues or through traveltime inversion of manually checked and picked DAS channels. In the latter procedure, a Markov chain Monte Carlo approach (McMC) was employed to estimate hypocentral parameters (Riva et al., 2024). All selected events are located within a distance of less than 100 km from the closest DAS channel, with magnitudes lower than 3.5. Table 1 and Figure 1 provide an

overview of the metadata for the selected events and the geometrical relations of the DAS deployments/events.

2.2 Data pre-processing and onset picking

A straightforward pre-processing procedure is applied to the raw event recordings. Specifically, it employs detrending, cosine tapering, and bandpass filtering. The frequency bands of the filter are chosen by using the ratio of the frequency spectra of the pre-event signal and the signal during the event. An automatic picking procedure (STA/LTA) is utilized to identify the first onsets and retrieve the arrival times at the triggered DAS channels, thus simulating an operational workflow for real-time monitoring (Fig. 2). The channels triggered in the automatic picking procedure are then used to compute the P-wave amplitudes and SNRs. Signal amplitude is estimated using a 2-s-long time window around the automatic pick to include the onset and mitigate picking uncertainties. SNRs are computed employing the same 2-s time windows before (noise) and after (signal) the automatic onset picking.

2.3 Signal amplitude and SNRs

The estimated amplitudes are subsequently corrected for geometrical spreading and anelastic attenuation and compared with the angle spanned by the FOC-source and local FOC azimuths and the theoretical cable sensitivity. The following relation is used to correct for amplitude decay with distance from the event:

$$A(r) = A0 \cdot r^{-1} e^{(-k \cdot r)} \qquad (1)$$

with

$$k = (pi \cdot f)/(Q \cdot v) \qquad (1.1)$$

Where $A0$ is original amplitude, r the distance, f the frequency [Hz], Q the quality factor and v = Vp the P-wave velocity. In this study, we set f as the average filtering frequency range, Q as constant = 150, and Vp to 6000 m/s. Although the quality factor and P-wave velocity may not represent the

perfect fit for each case study, we prefer to remove a possible source of variability by setting constant values for all the different experiments. Moreover, prior information on the geological contexts, and thus on the above-mentioned parameters, is known only for a few cable deployments.

To account for potential variations in onset amplitudes resulting from signal polarization along the array, we compute the theoretical local axial sensitivity of the cable. Initially, FOC-event and FOC azimuths are computed by determining, for each channel, the direction to the next neighbouring channel along the cable. This information is used to compute theoretical sensitivities for each event-DAS geometry pair, following the formulation described in Martin et al., (2021), under the plane wave assumption and for P-waves:

$$THsens = a \cdot b \cdot c \cdot d \quad (2)$$

with:

$$a = \frac{(2 \cdot v \cdot k)}{g} \quad (2.1)$$

$$b = cos(\alpha) \quad (2.2)$$

$$c = cos(\beta) \quad (2.3)$$

$$d = sin(0.5 \cdot (g \cdot k \cdot cos(\alpha) \cdot cos(\beta)) \quad (2.4)$$

Where v = Vp is the P-wave velocity, k the wavenumber, g the gauge length, α the ray path azimuth and β the ray path dip angle. In this study, we set Vp = 6000 m/s. Although the plane wave assumption may not universally apply in all case studies, theoretical sensitivities are expected to exhibit a first-level correlation with signal amplitudes, particularly when correcting for distance decay. We normalize the theoretical sensitivities to the maximum expected value. Thus, when the azimuth is 90° and/or the dip angle is 90°, the value is set to 0, while in the opposite case, it is set to 1. This preliminary analysis aims to explore whether azimuthal sensitivity significantly influences signal amplitudes or if other more complex, and difficult-to-model, factors (e.g., site conditions and cable coupling) exert a more substantial impact. Source radiation patterns may also contribute to defining amplitude variations along the array. However, this feature was not modelled in the work due to a lack of information on source parameters for specific cases. Nonetheless, we consider possible sine-like amplitude variations along the array in the interpretation phase.

We analyze the spatial variations of onset amplitudes by plotting these values against the incidence angle, and we supplement the information with theoretical sensitivity data (Fig. 3-4-5).

2.3 Waveform correlation

The second part of the study focuses on the spatial coherence of recorded waveforms. The same filtering procedures (i.e., detrending and bandpass filtering) outlined above were adopted as a pre-processing step. We computed cross-correlation functions for all possible DAS channel pairs, using the same time window considered for SNR computation. For selected case studies, we plotted the matrix of the Maxima of the Cross-Correlation functions (MCCs). This matrix is useful for highlighting the spatial distribution of correlation. Additionally, the MCCs were evaluated in their dependence on the interchannel distance and the SNRs.
Finally, the decay of correlation with interchannel distance is compared to what is predicted by the theory (after Menke et al., 1990), limiting the analysis to 100 m for clarity:

$$MCCij = e^{\left(-\frac{k*Rij}{\lambda}\right)} \qquad (3)$$

Where k= 2-3, Rij is the interchannel distance between channel i and j and λ is the wavelength. In this study, we set k=2.5 and we compute λ from a fixed P-wave velocity of 6000 m/s and the average filtering frequency range.
To examine the spatial distribution of waveform correlation, we intentionally eliminate possible angular dependencies, i.e., azimuth and radiation pattern. Indeed, for six specific case studies (MONTEREY, CANARY, STANFORD-2, FORESEE, GRÍMSVÖTN, POROTOMO) we identify a rectilinear portion of the cable comprising 100 channels, favourably oriented with respect to the incidence angle (avoiding perpendicular incidence which in theory should be poorly sensed). This approach, unlike the analysis presented in Section 3.1, proves to be feasible for waveform correlation due to the abundance of potential DAS channel pairs, even within a limited selection of the cable. Indeed, e.g., for 100 channels, we end up potentially with 4950 estimates of MCCs.

We analyze the spatial variations of waveform correlation by plotting MCCs against the interchannel distance, and we supplement the information with the values expected from theory (Menke et al., 1990). For each case study, we dedicate a figure (Fig. 6, 7, 8, 9, 10, 11).

3 Results

3.1 Spatial distribution of onset amplitudes

Figures 3, 4 and 5 show the observed onset amplitudes, corrected for geometrical spreading and attenuation, in relation to the azimuth and the theoretical sensitivity. A subset of case studies (HCMR, MONTEREY, HENGILL-GFZ, GRÍMSVÖTN), yet cristal clear only in MONTEREY, exhibits a first-order influence of the incidence angle and, consequently, of the theoretical sensitivity, on onset amplitudes (Fig. 3a, 3b, 4f, 5d). However, NESTOR, MEUST, and RHONEGLETSCHER case studies show an opposite, yet weak, behaviour (Fig. 3c, 3d, 5b). No clear dependences on the incidence angle are observed for all other case studies (Fig. 3e, 4b, 4c, 4d, 4e, 5a, 5c). Notably, amplitude variations related to the incidence angle are 1-2 orders of magnitude lower than the observed scattering for fixed azimuth. Indeed, after correcting the amplitudes for the decay with epicentral distance (eq. 1), the residuals should in principle reflect the influence of both signal polarization along the array and/or radiation pattern from the source, which is not coherently visible from our results. While we cannot completely rule out the source effects, due to a lack of prior information, we observe a lack of generalized and simple correlation with the incidence angle, in favour of more complex dependencies.

3.2 Spatial distribution of waveform correlation

Figures 6, 7, 8, 9, 10 and 11 present an overview of the spatial distribution of waveform correlation for six selected case studies, MONTEREY, CANARY, STANFORD-2, FORESEE, GRÍMSVÖTN, POROTOMO, two for each installation environment. The orange sections on the cables (Fig. 6a, 7a, 8a, 9a, 10a, 11a) indicate the chosen 100 channels for the analysis. Additionally, we display the automatic picks and record sections, providing the timing of the event onsets (Fig. 6b, 7b, 8b, 9b, 10b, 11b). We draw attention to the fact that not all channels are triggered, which is expected, given the automatic picking procedure (STA-LTA) employed for the study. As a consequence, the resulting amount of onset time estimates are slightly different among the different case studies. The reader can refer to Figure 2 for the complete recording of the events.

As expected, the MCC matrices (Fig. 6c, 7c, 8c, 9c, 10c, 11c) display a concentration of high values along the diagonal (corresponding to small interchannel distances). MCCs then decrease, yet irregularly, with increasing interchannel distance (Fig. 6d, 7d, 8d, 9d, 10d, 11d). Similar to the analysis of spatial amplitude variations, complex variations of MMC dependencies emerge (Fig. 6d, 9d, 10d), such as sudden increases at higher interchannel distances. Furthermore, the scattering of MCCs is more pronounced than the aforementioned first and second-order variations, with the notable exception of POROTOMO. When comparing the MCCs with the expected trend (Menke et al., 1990), in most cases we observe that the observed MCCs decay with inter-channel distance is much faster than what predicted by the theory. A noteworthy exception is represented by the GRÍMSVÖTN case study, for which our measurements are consistent with the predictions in the sense of eq. (2). This is

likely attributed to the unique installation environment, consisting of a glacier with a thickness of hundreds of meters (Klaasen et al., 2023). This confirms that medium homogeneity plays a crucial role in controlling the quality and consistency of DAS recordings.

As expected, MCCs generally exhibit a positive correlation with onset SNRs. Thus, in the cable sections where the event emerges more clearly from the background noise, the recordings are also more coherent each other.

4 Discussion

The analysis of spatial variations in onset amplitudes across different experimental setups suggests that signal polarization along the cable alone cannot fully explain the observed scattering (Fig. 3-4-5). For DAS segments with a similar azimuth in relation to the event, the span of amplitude variations is up to two orders of magnitude larger than what predicted by theory for the incidence angle dependency throughout the whole cable. The expected influence of the source radiation pattern should yield a sine-like amplitude modulation with the incidence angle, but those effects are not clearly visible in our results. Our findings thus indicate that the observed amplitude modulation are mostly controlled by other, non-predictable factors, such as local velocity heterogeneities (Piana Agostinetti et al., 2022; Jousset et al., 2018; Lior et al., 2021) and variations in cable coupling (Celli et al., 2023; Miller et al., 2018). These effects affect particularly shallow-horizontal arrays, while may be less important for data acquired in wells. Nevertheless, monitoring seismicity with DAS in wells might provide insufficient azimuthal direction coverage for constraining event location (while being more efficient for signal detection). Hence, when exploiting superficial DAS arrays for similar purposes, we should take into account the likely occurrence of significant amplitude modulations with complex spatial patterns.

Obtaining prior information on local velocity heterogeneities and cable coupling or modeling their influence is challenging, especially for commercial telecommunication cables (submarine environments or urban contexts). Therefore, in evaluating a DAS experiment, significant attention should be paid to understanding and possibly isolating the cable portions showing these undesired signal amplitude decays.

In several seismological analyses, such as location or source mechanism inversion, it is common practice to select or weight stations based on their inferred distance from the source and, additionally,

SNRs. While we know that DAS recording amplitudes do not exclusively correlate with the distance from the source (due to azimuthal sensitivity), our results highlight other, more complex and stronger effects. Therefore, relying solely on distance-based processing techniques for DAS arrays is insufficient. Instead, greater emphasis should be placed on developing tailored workflows that consider the specific noise distribution of the FOC.

The analysis of spatial variability in waveform correlation highlights complex dependencies with interchannel distance (Fig. 6, 7, 8, 9, 10 and 11), confirming the strong dependence of DAS performance on local velocity anomalies and/or cable coupling inhomogeneities (Van den Ende and Ampuero, 2021). Consequently, when utilizing local waveform coherence for array techniques based on differential travel times, careful data selection is essential to avoid mixing phase information and/or obtaining meaningless estimates from poorly correlated channel pairs. A prior assessment of SNRs, associated with a strong limitation of the exploited interchannel distance and proper weighting of the measured delay times, can provide useful constraints for this task. However, this may limit the actual aperture of the resulting sub-array (i.e., the virtual deployment composed of only well-correlated channels), potentially compromising the performance of the sub-array in terms of Direction of Arrival (DOA) and apparent velocity estimations. On a positive note, the unprecedented sampling density provided by DAS technology usually allows for a sufficient amount of measurement points, even when a strong selection of arrival times is employed.

Conclusions

This study examined 15 local events (purely tectonic, volcano-tectonic, and ice-quakes) recorded with DAS technology in various installation environments to evaluate the spatial distributions of onset amplitudes and waveform correlation. Having in mind a seismological monitoring framework, we estimated the onset timing of these events using STA-LTA after a standard waveform processing. Subsequently, we conducted a detailed analysis of P-wave amplitudes, correcting for geometrical spreading and anelastic attenuation. We examined the relative importance of intrinsic and modelable features, that is theoretical cable sensitivity, and more complex, difficult-to-predict site-dependent properties, on amplitudes spatial variation. Following this, in line with another data type commonly used in seismic monitoring, that is phase differential arrival times, we performed a study on waveform coherency (from multichannel cross-correlation) for selected rectilinear and well-oriented cable portions, thus mitigating the angular dependencies. The Maxima of the Cross-Correlation functions

(MCCs) were evaluated against the interchannel distance, following routine procedures used with seismological arrays, and were compared with expected values.

Our findings underscore how DAS recordings exhibit complex spatial patterns, which deviate from the predictions, in both onset amplitudes and waveform correlation, possibly impacting estimates of absolute and differential arrival times. Our findings indicate that these variations are difficult to model, as they predominantly depend on factors that are difficult or impossible to evaluate a priori, e.g. coupling and local velocity structure. As a matter of fact, we observed that axial sensitivity or interchannel distance, which can be evaluated a priori, are not acting alone in influencing real data amplitude and shape variations.

We thus conclude that utilization of recordings from shallow-horizontal DAS deployments for hypocentral location should be preceded by rigorous channel selection and weighting procedures, to be tailored to the waveform characteristics of the specific experiment. On a positive note, there is significant potential in harnessing the abundance of data points to develop smart procedures for extracting meaningful information. This evaluation should complement, rather than substitute, traditional geometrical studies on the network's potential for monitoring seismicity.

Acknowledgements

Authors are grateful to the following researchers and institutions for their contributions to the datasets analyzed in this study: Alan Baird (NORSAR, Kjeller, Norway); Biondo Biondi and Siyuan Yuan (Stanford University); Nate Lindsey (FiberSense™); Arantza Ugalde, (Barcelona Center for Subsurface Imaging, Barcelona, Spain); CANALINK-Canarias submarine link S.L. (http://www.canalink.tel), part of the group Instituto Tecnológico y de Energías Renovables (ITER) and Cabildo de Tenerife.

Bibliography

Ajo-Franklin J. B., Dou S., Lindsey N. J., Monga I., Tracy C., Robertson M., Tribaldos Rodriguez V., Ulrich C., Freifeld B., Daley T. and Li X.; 2019: *Distributed acoustic sensing using dark fiber for near-surface characterization and broadband seismic event detection*. Scientific reports, 9(1), 1328.

Allen R.; 1982: *Automatic phase pickers: Their present use and future prospect*s. Bulletin of the Seismological Society of America, 72(6B), S225-S242.

Biagioli F., Métaxian J. P., Stutzmann E., Ripepe M., Bernard P., Trabattoni A., Longo R. and Bouin M. P., 2024: *Array analysis of seismo-volcanic activity with distributed acoustic sensing*. Geophysical Journal International, 236(1), 607-620.

Biondi B. L., Yuan S., Martin E. R., Huot F. and Clapp R. G.;2021: *Using telecommunication fiber infrastructure for earthquake monitoring and near‐surface characterization.* Distributed Acoustic Sensing in Geophysics: Methods and Applications, 131-148.

Biondi E., Zhu W., Li J., Williams E. F. and Zhan, Z.; 2023: *An upper-crust lid over the Long Valley magma chamber*. Science Advances, 9(42), eadi9878.

Cannon R. and Aminzadeh F.; 2013. *Distributed acoustic sensing: State of the art.* SPE Digital Energy Conference and Exhibition (pp. SPE-163688).

Celli N. L., Bean C. J. and O'Brien G. S.; 2024: *Full-waveform simulation of DAS records, response and cable-ground coupling*. Geophysical Journal International, 236(1), 659-674.

Cheng F., Chi B., Lindsey N. J., Dawe T. C. and Ajo-Franklin J. B.; 2021: *Utilizing distributed acoustic sensing and ocean bottom fiber optic cables for submarine structural characterization*. Scientific reports, 11(1), 5613.

Feigl K.; 1969: *PoroTomo natural laboratory horizontal and vertical distributed acoustic sensing data* (No. 980). USDOE Geothermal Data Repository (United States); Univ. of Wisconsin, Madison, WI (United States).

Fernández-Ruiz M. R., Martins H. F., Williams E. F., Becerril C., Magalhães R., Costa L., Lopez M. L., Jia Z., Zhan Z and González-Herráez, M.; 2022: *Seismic monitoring with distributed acoustic sensing from the near-surface to the deep oceans*. Journal of Lightwave Technology, 40(5), 1453-1463.

Fichtner A., Klaasen S., Thrastarson S., Çubuk‐Sabuncu Y., Paitz P. and Jónsdóttir K.; 2022: *Fiber‐optic observation of volcanic tremor through floating ice sheet resonance*. The Seismic Record, 2(3), 148-155.

Güemes A., Fernández-López A. and Soller B.; 2010: *Optical fiber distributed sensing-physical principles and applications*. Structural Health Monitoring, 9(3), 233-245.

Jousset P., Reinsch T., Ryberg T., Blanck H., Clarke A., Aghayev R., Hersir G. P., Henninges J., Weber M. and Krawczyk, C. M.; 2018: *Dynamic strain determination using fibre-optic cables allows imaging of seismological and structural features*. Nature communications, 9(1), 2509.

Jousset P., Currenti G., Schwarz B., Chalari A., Tilmann F., Reinsch T., Zuccarello L., Privitera E. and Krawczyk, C. M.; 2022: *Fibre optic distributed acoustic sensing of volcanic events*. Nature communications, 13(1), 1753.

Karrenbach M., Cole S., Ridge A., Boone K., Kahn D., Rich J., Silver K. and Langton, D.; 2019: *Fiber-optic distributed acoustic sensing of microseismicity, strain and temperature during hydraulic fracturing*. Geophysics, 84(1), D11-D23.

Klaasen S., Paitz P., Lindner N., Dettmer J. and Fichtner A.; 2021: *Distributed acoustic sensing in volcano‐glacial environments—Mount Meager, British Columbia*. Journal of Geophysical Research: Solid Earth, 126(11), e2021JB022358.

Klaasen S., Thrastarson S., Çubuk-Sabuncu Y., Jónsdóttir K., Gebraad L., Paitz P. and Fichtner, A.; 2023: *Subglacial volcano monitoring with fibre-optic sensing: Grímsvötn, Iceland*. Volcanica, 6(2), 301-311.

Kennett B. L.; 2022: *The seismic wavefield as seen by distributed acoustic sensing arrays: local, regional and teleseismic sources*. Proceedings of the Royal Society A, 478(2258), 20210812.

Li Z., Shen Z., Yang Y., Williams E., Wang X. and Zhan Z; 2021: *Rapid response to the 2019 Ridgecrest earthquake with distributed acoustic sensing*. AGU Advances, 2(2), e2021AV000395.

Li J., Zhu W., Biondi E. and Zhan Z.; 2023: *Earthquake focal mechanisms with distributed acoustic sensing.* Nature Communications, 14(1), 4181.

Lellouch A., Lindsey N. J., Ellsworth W. L. and Biondi B. L.; 2020: *Comparison between distributed acoustic sensing and geophones: Downhole microseismic monitoring of the FORGE geothermal experiment*. Seismological Society of America, 91(6), 3256-3268.

Lindsey N. J., Martin E. R., Dreger D. S., Freifeld B., Cole S., James S. R., Biondi B. L. and Ajo‐Franklin J. B; 2017: *Fiber‐optic network observations of earthquake wavefields*. Geophysical Research Letters, 44(23), 11-792.

Lindsey N. J., Dawe T. C. and Ajo-Franklin J. B.; 2019: *Illuminating seafloor faults and ocean dynamics with dark fiber distributed acoustic sensing.* Science, 366(6469), 1103-1107.

Lindsey N. J., Rademacher H. and Ajo‐Franklin J. B; 2020: *On the broadband instrument response of fiber‐optic DAS arrays*. Journal of Geophysical Research: Solid Earth, 125(2), e2019JB018145.

Lior I., Sladen A., Mercerat D., Ampuero J. P., Rivet D. and Sambolian S; 2021: *Strain to ground motion conversion of distributed acoustic sensing data for earthquake magnitude and stress drop determination*. Solid Earth, 12(6), 1421-1442.

Lior I., Mercerat E. D., Rivet D., Sladen A. and Ampuero J. P.; 2022: *Imaging an underwater basin and its resonance modes using optical fiber distributed acoustic sensing*. Seismological Society of America, 93(3), 1573-1584.

Martin E. R., Lindsey N. J., Ajo‐Franklin J. B. and Biondi, B. L.; 2021: *Introduction to interferometry of fiber‐optic strain measurements*. Distributed Acoustic Sensing in Geophysics: Methods and Applications, 111-129.

Mateeva A., Mestayer J., Cox B., Kiyashchenko D., Wills P., Lopez S. J., Hornman K., Lumens P., Franzen A., Hill D. and Roy J.; 2012: *Advances in distributed acoustic sensing (DAS) for VSP*. SEG Technical Program Expanded Abstracts 2012 (pp. 1-5). Society of Exploration Geophysicists.

Menke W., Lerner-Lam A. L., Dubendorff B. and Pacheco J.; 1990: *Polarization and coherence of 5 to 30 Hz seismic wave fields at a hard-rock site and their relevance to velocity heterogeneities in the crust*. Bulletin of the Seismological Society of America, 80(2), 430-449.

Mestayer J., Cox B., Wills P., Kiyashchenko D., Lopez J., Costello M., Bourne S., Ugueto G., Lupton R., Solano G., Hill D. and Lewis A.; 2011: *Field trials of distributed acoustic sensing for geophysical monitoring.* Seg technical program expanded abstracts 2011 (pp. 4253-4257). Society of Exploration Geophysicists.

Miller, D. E., Coleman T., Zeng X., Patterson J. R., Reinisch E. C., Cardiff M. A., Wang H. F., Fratte D., Trainor-Guitton W., Thurber C. H., Robertson M. and Feigl K.; 2018: *DAS and DTS at Brady Hot*

Springs: Observations about coupling and coupled interpretations. Proceedings of the 43rd Workshop on Geothermal Reservoir Engineering, Stanford, CA, USA (pp. 12-14).

Molenaar M. M., Hill D., Webster P., Fidan E. and Birch, B.; 2011: *First downhole application of distributed acoustic sensing (DAS) for hydraulic fracturing monitoring and diagnostics*. SPE Hydraulic Fracturing Technology Conference and Exhibition (pp. SPE-140561). SPE.

Nishimura T., Emoto K., Nakahara H., Miura S., Yamamoto M., Sugimura S., Ishikawa A. and Kimura T.; 2021: *Source location of volcanic earthquakes and subsurface characterization using fiber-optic cable and distributed acoustic sensing system*. Scientific reports, 11(1), 6319.

Obermann A., Sánchez‐Pastor P., Wu S. M., Wollin C., Baird A. F., Isken M. P., Clinton J., Goertz‐Allmann B. P., Dahm T., Wuestefeld A., Shi P., Lanza F.; Gyger L., Wetter S., Hjörleifsdóttir V., Langet N., Brynjarsson B., Jousset P. and Wiemer S; 2022: *Combined Large‐N Seismic Arrays and DAS Fiber Optic Cables across the Hengill Geothermal Field, Iceland*. Seismological Society of America, 93(5), 2498-2514.

Parker T., Shatalin S. and Farhadiroushan M.; 2014: *Distributed Acoustic Sensing–a new tool for seismic applications*. first break, 32(2).

Piana Agostinetti N., Villa A. and Saccorotti G.; 2022: *Distributed acoustic sensing as a tool for subsurface mapping and seismic event monitoring: A proof of concept.* Solid Earth, 13(2), 449-468.

Porras J., Pecci D., Bocchini G. M., Gaviano S., De Solda M., Tuinstra K., Lanza F., Tognarelli A., Stucchi E. and Grigoli F.; 2024: *A semblance-based microseismic event detector for DAS data*. Geophysical Journal International, 236(3), 1716-1727.

Riva F., Agostinetti N. P., Marzorati S. and Horan C.; 2024: *The micro‐seismicity of Co. Donegal (Ireland): Defining baseline seismicity in a region of slow lithospheric deformation.* Terra Nova, 36(1), 62-76.

Rost S. and Thomas C.; 2002: *Array seismology: Methods and applications*. Reviews of geophysics, 40(3), 2-1.

Shen J. and Zhu, T.; 2021: *Seismic noise recorded by telecommunication fiber optics reveals the impact of COVID‐19 measures on human activity*. The Seismic Record, 1(1), 46-55.

Spica Z. J., Ajo‐Franklin J., Beroza G. C., Biondi B., Cheng F., Gaite B., Luo B., Martin E., Shen J., Thurber C., Viens L., Wang H., Wuestefeld A., Xhiao H. and Zhu T.; 2023: *PubDAS: A PUBlic Distributed Acoustic Sensing Datasets Repository for Geosciences*. Seismological Society of America, 94(2A), 983-998.

Trabattoni A., Festa G., Longo R., Bernard P., Plantier G., Zollo A. and Strollo A.; 2022: *Microseismicity monitoring and site characterization with distributed acoustic sensing (DAS): The case of the Irpinia fault system (Southern Italy)*. Journal of Geophysical Research: Solid Earth, 127(9), e2022JB024529.

Trabattoni A., Biagioli F., Strumia C., Van den Ende M., Scotto di Uccio F., Festa G., Rivet D., Sladen A., Ampuero J. P., Métaxian J. P. and Stutzmann E.; 2023: *From strain to displacement: using deformation to enhance distributed acoustic sensing applications.* Geophysical Journal International, 235(3), 2372-2384.

Ugalde A., Becerril C., Villaseñor A., Ranero C. R., Fernández‐Ruiz M. R., Martin‐Lopez S., González‐Herráez M. and Martins H. F.; 2022: *Noise levels and signals observed on submarine fibers in the Canary Islands using DAS*. Seismological Society of America, 93(1), 351-363.

Van den Ende M. P. and Ampuero, J. P.; 2021: *Evaluating seismic beamforming capabilities of distributed acoustic sensing arrays*. Solid Earth, 12(4), 915-934.

Villasenor A., Ugalde A., Gonzalez-Herraez M., Martins H., and Cosin M.; 2020: *Canary Islands seismic monitoring with Distributed Acoustic Sensing* [Data set]. International Federation of Digital Seismograph Networks.

Walter F., Gräff D., Lindner F., Paitz P., Köpfli M., Chmiel M. and Fichtner, A; 2020: *Distributed acoustic sensing of microseismic sources and wave propagation in glaciated terrain*. Nature communications, 11(1), 2436.

Wuestefeld A, Spica J. S., Aderhold K., Huang H. H., Ma K., Lai V. H., Miller M., Urmantseva L., Zapf D., Bowden D. C., Edme P., Kiers T., Rinaldi A. P., Tuinstra K., Jestin C., Diaz‐Meza S., Jousset P., Wollin C., Ugalde A., Gaite S. R. B., Currenti G., Prestifilippo M., Araki E., Tonegawa T., Ridder S., Nowacki A., Lindner F., Schoenball M., Wetter C., Zhu H., Baird A. F., Rørstadbotnen R. A., Ajo‐Franklin J., Ma Y., Abbott R. E., Hodgkinson K. M., Porritt R. W., Stanciu C., Podrasky A., Hill D., Biondi B., Yuan S., Luo B., Nikitin S., Morten J. P., Dumitru V. A., Lienhart W., Cunningham E., Wang E.; 2023: *The Global DAS Month of February 2023.* Seismological Research Letters.

Yang Y., Atterholt J. W., Shen Z., Muir J. B., Williams E. F. and Zhan, Z.; 2022: *Sub‐kilometer correlation between near‐surface structure and ground motion measured with distributed acoustic sensing.* Geophysical Research Letters, 49(1), e2021GL096503.

Yuan S., Lellouch A., Clapp R. G. and Biondi B.; 2020: *Near-surface characterization using a roadside distributed acoustic sensing array*. The Leading Edge, 39(9), 646-653.

Zhan Z.; 2020: *Distributed acoustic sensing turns fiber‐optic cables into sensitive seismic antennas.* Seismological Research Letters, 91(1), 1-15.

Zhu T., Shen J. and Martin E. R.; 2020: *Sensing Earth and environment dynamics by telecommunication fiber-optic sensors: An urban experiment in Pennsylvania USA*. Solid Earth Discussions, 2020, 1-30.

Tables and Figures

Array context	DAS ID	Location	Cable length [km]	N° of channels (gauge length, ch. Spacing)	Event distance [Km]	Event info (magnitude if known)
Submarine telecom.	HCMR	Greece	26.2	688 (19.2,19.2)	99.7	M 2.0
Submarine telecom.	MONTEREY	California [USA]	19.9	6001 (10,2)	34.5	M 3.4
Submarine telecom.	NESTOR	Greece	26.2	1365 (19.2,19.2)	29.6	M 2.0
Submarine telecom.	MEUST	France	44.8	4480 (19.2,19.2)	88.8	M 2.4
Submarine telecom.	CANARY	Canary Islands [SP]	59.8	5983 (10,10)	44.2	M 3.1
Terrestrial telecom.	STANFORD-1	California [USA]	2.6	626 (8.16,4.08)	3.9	M 2.0
Terrestrial telecom.	STANFORD-2	California [USA]	2.8	353 (16,8)	10.4	M 2.0
Terrestrial telecom.	FORESEE	Pennsylvania [USA]	4.9	2432 (10,2)	20.7	Earthquake M. 1.1
Terrestrial telecom.	AZUMA-VOLCANO	Japan	14.3	1404 (40.8,10.2)	0.6	Volcanic earthquake M –0.1
Terrestrial telecom.	HENGILL-NORSAR	Iceland	34.8	1742 (20,10)	9.3	Earthquake, geothermal area [no catalogue magnitude]
Terrestrial telecom.	HENGILL-GFZ	Iceland	14.6	3648 (6,3)	5.6	Earthquake, geothermal area [no catalogue magnitude]
Fit-for-purpose	RHONEGLETSCHER	Switzerland	1.7	422 (8,4)	0.8	Ice-quake [no catalogue magnitude]
Fit-for-purpose	MOUNT-MEAGER	Canada	3	380 (8,8)	2.8	Ice-quake [no catalogue magnitude]
Fit-for-purpose	POROTOMO	Nevada [USA]	8.6	8620 (10,1)	0.3	Earthquake, geothermal plant [no catalogue magnitude]
Fit-for-purpose	GRÍMSVÖTN	Iceland	14.1	1728 (8.16,8.16)	1.8	Earthquake, volcano caldera [no catalogue magnitude]

Table 1. Metadata of the DAS deployments and selected events.

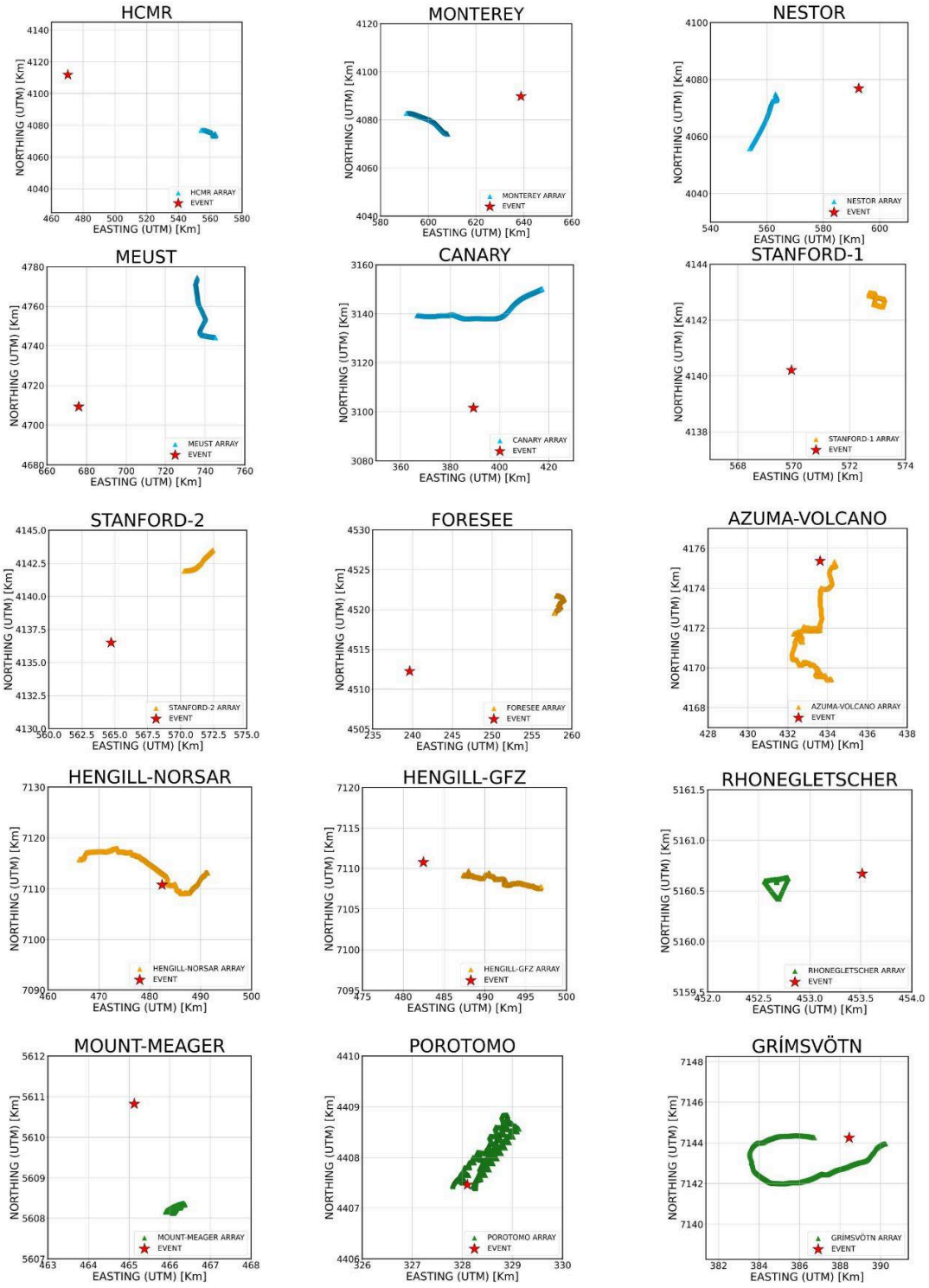

Figure 1. Datasets analyzed in the study: list of DAS array geometries and event locations.

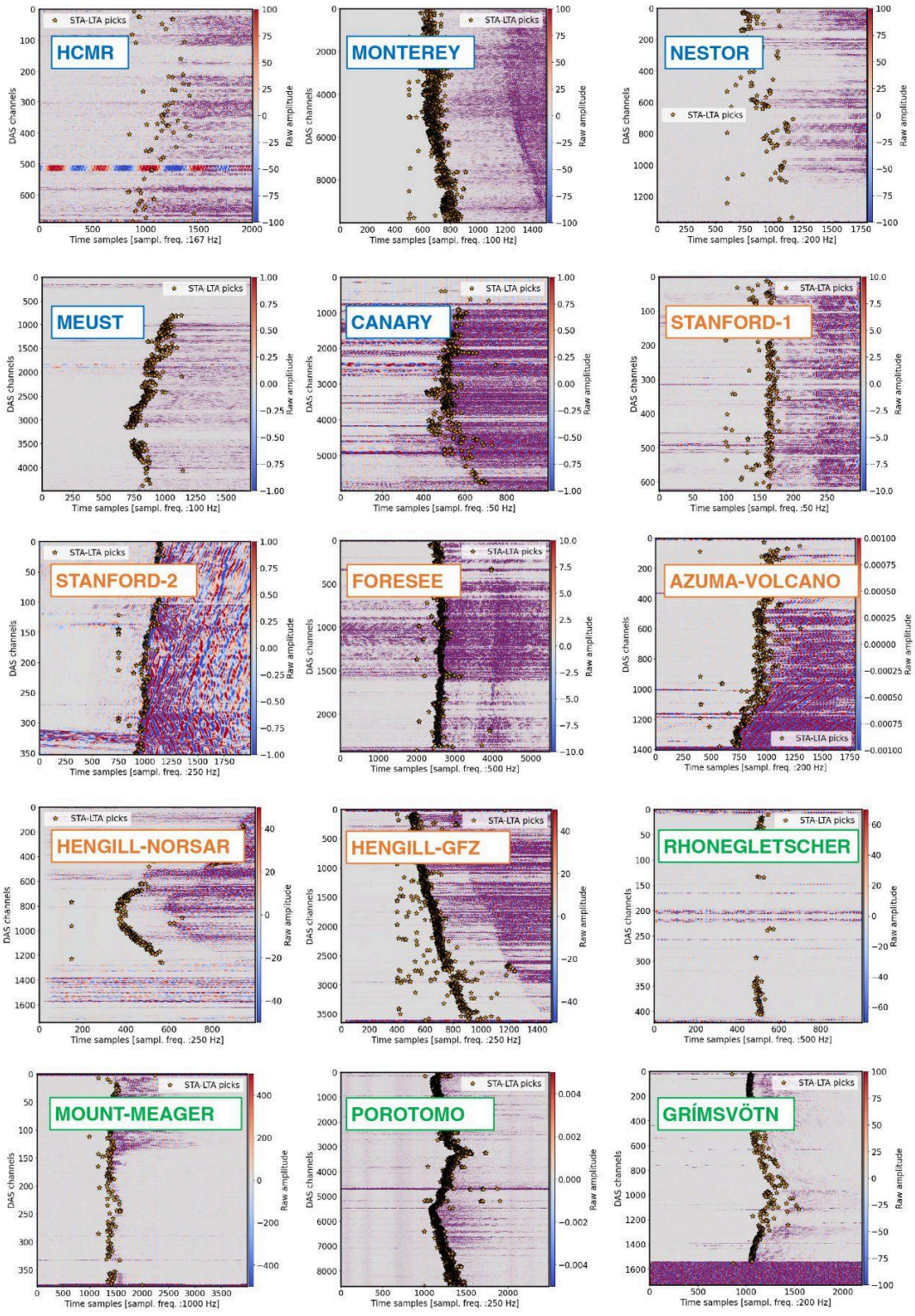

Figure 2. Recorded events and STA-LTA onset picks.

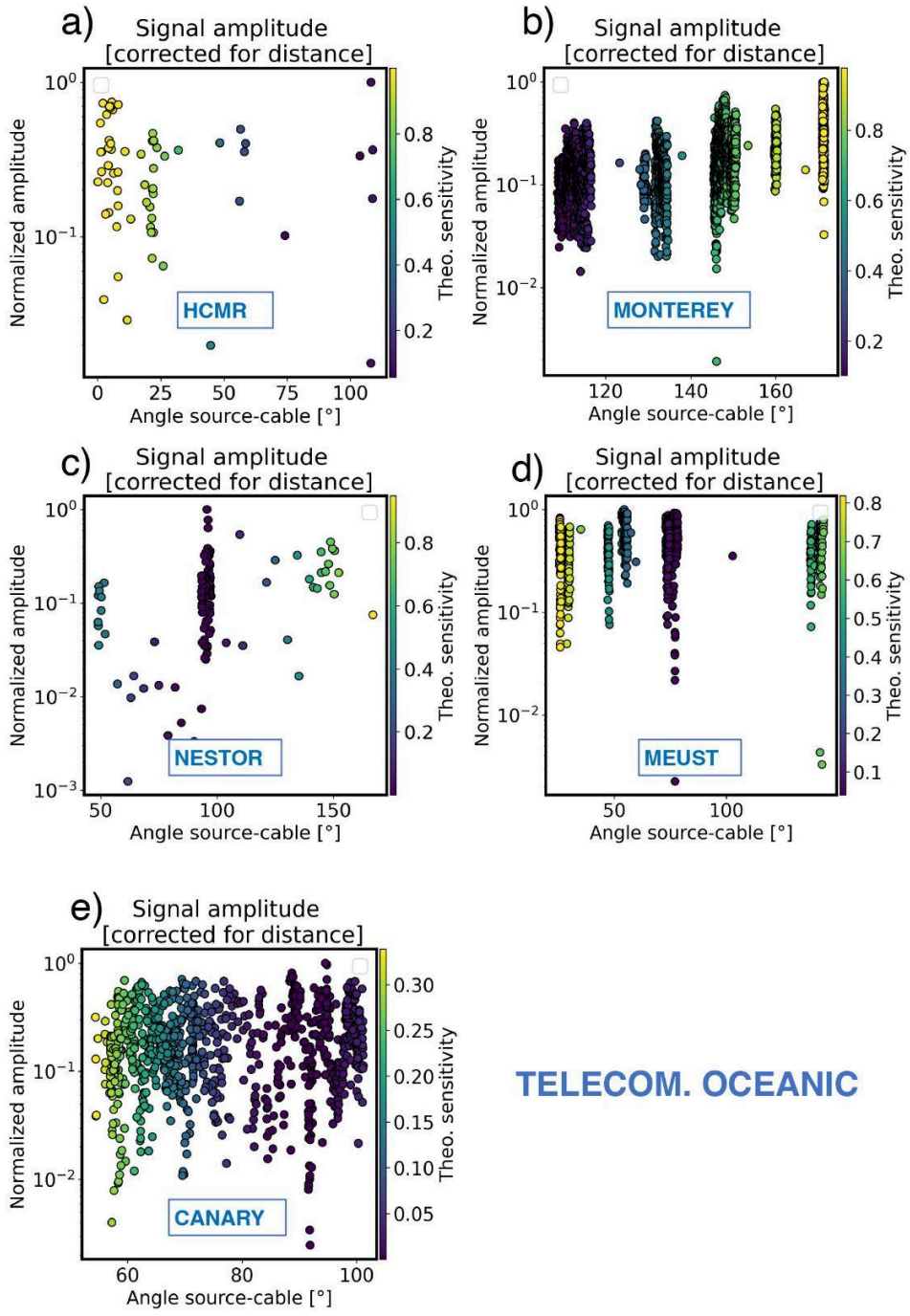

Figure 3. Telecommunication oceanic FOCs. Onset amplitudes (normalized for geometrical spreading effects) against incidence angle. Theoretical sensitivity values are overplotted over data points using a scale of colors.

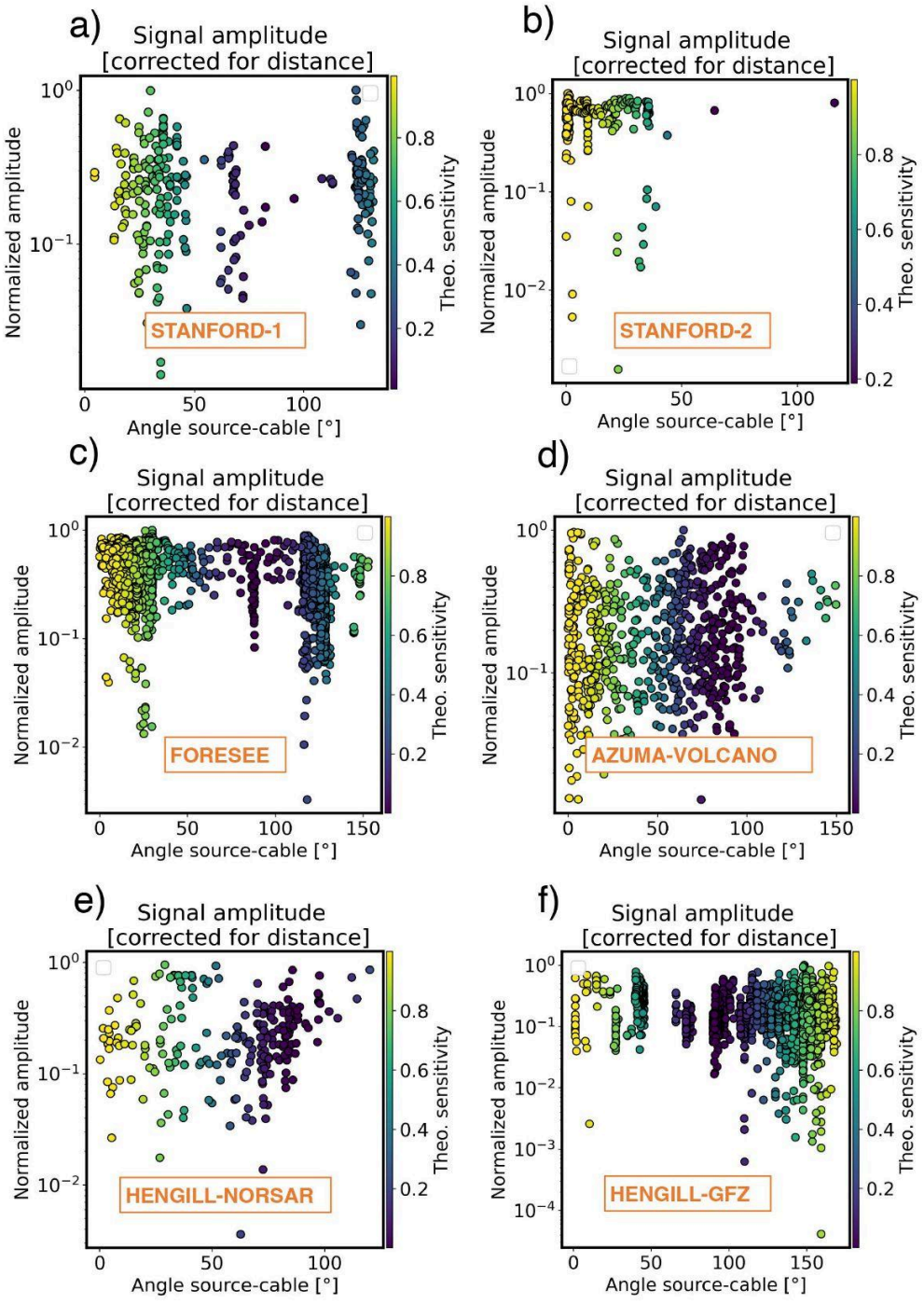

Figure 4. Telecommunication terrestrial FOCs. Onset amplitudes (normalized for geometrical speading effects) against incidence angle. Theoretical sensitivity values are overplotted over data points using a scale of colors.

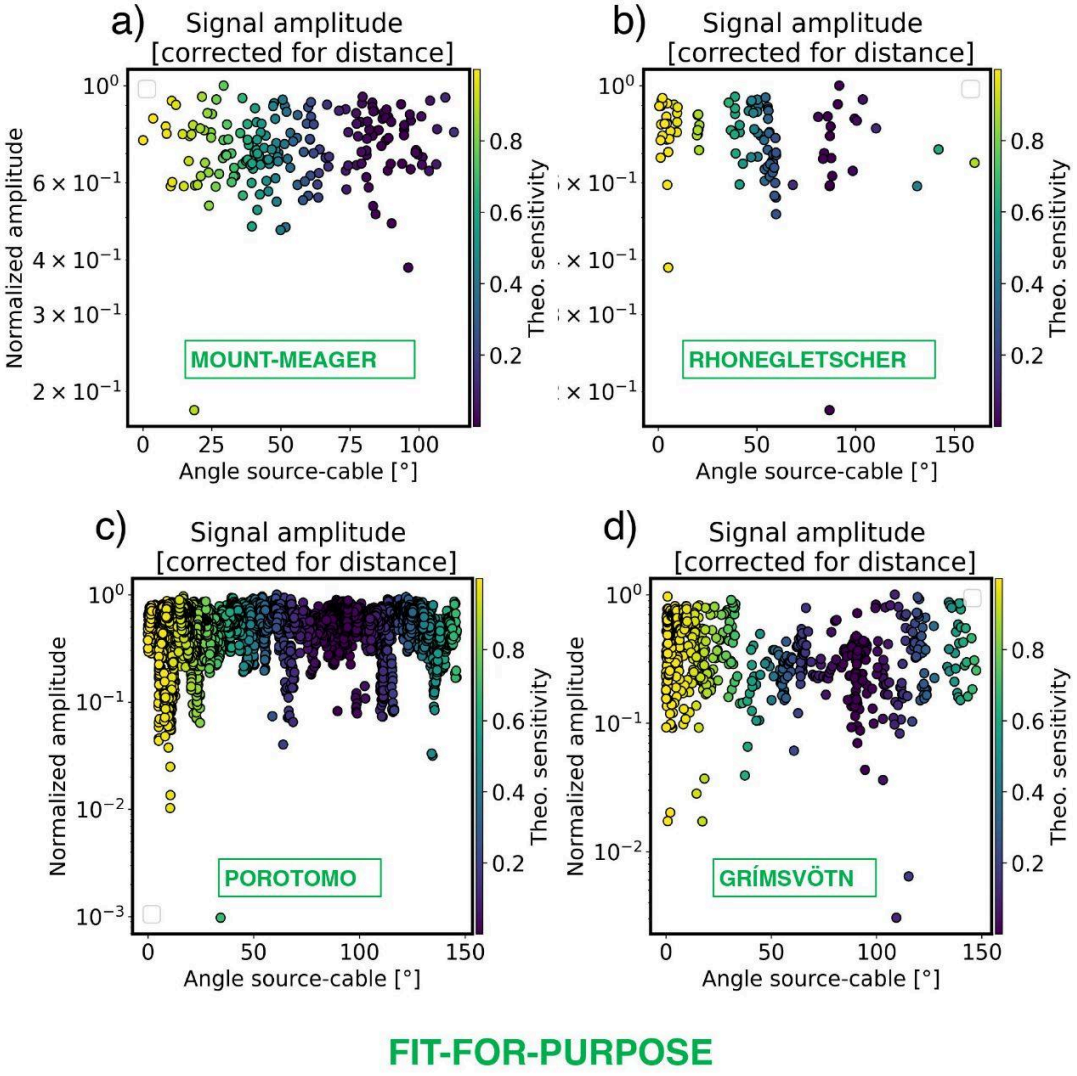

Figure 5. "Fit-for-purpose" FOCs. Onset amplitudes (normalized for geometrical speading effects) against incidence angle. Theoretical sensitivity values are overplotted over data points using a scale of colors.

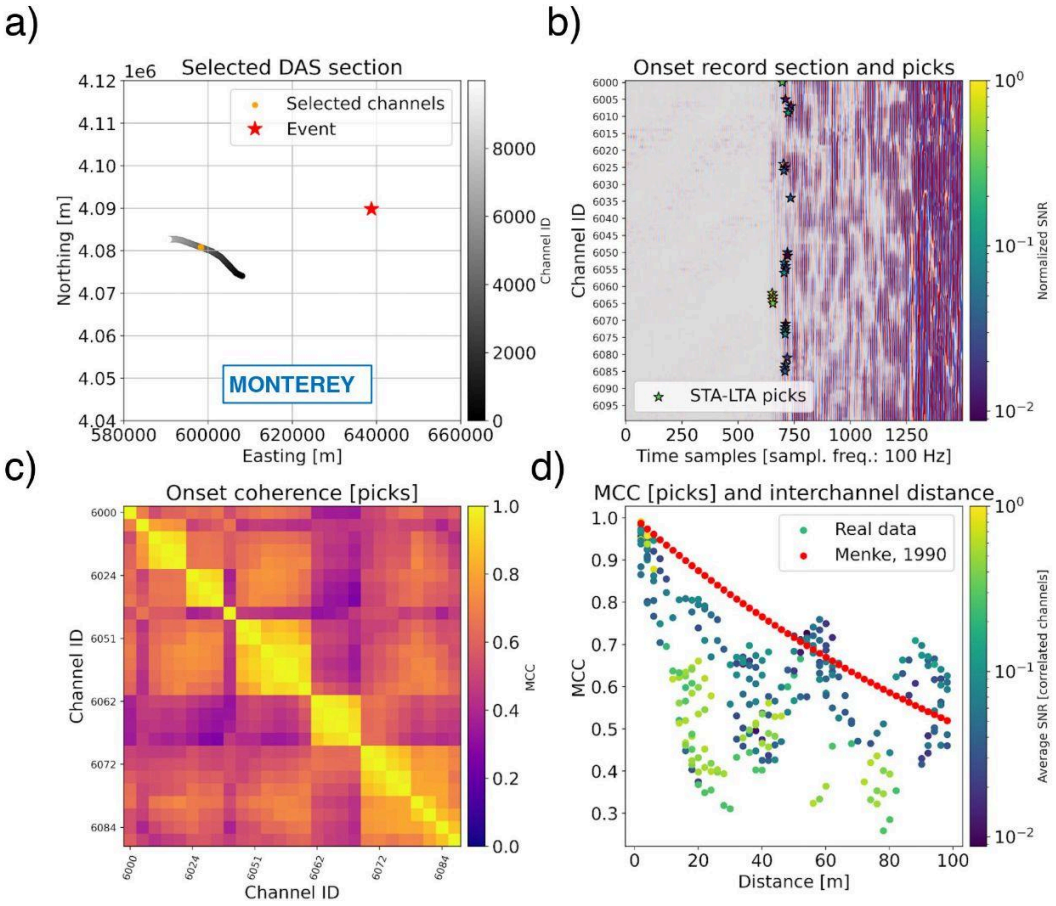

Figure 6. Waveform Correlation Analysis: MONTEREY case study. a) Selected rectilinear portion; b) Onset record section and triggered channels associated with SNRs (STA-LTA picks as colored stars); c) MCCi matrix for the picked channels; d) MCCi against interchannel distance, limited to 100 m. The average SNRs for the cross-correlated channels are shown with a scale of colors. A theoretical decay, following Menke et al., 1990, is provided as red dots.

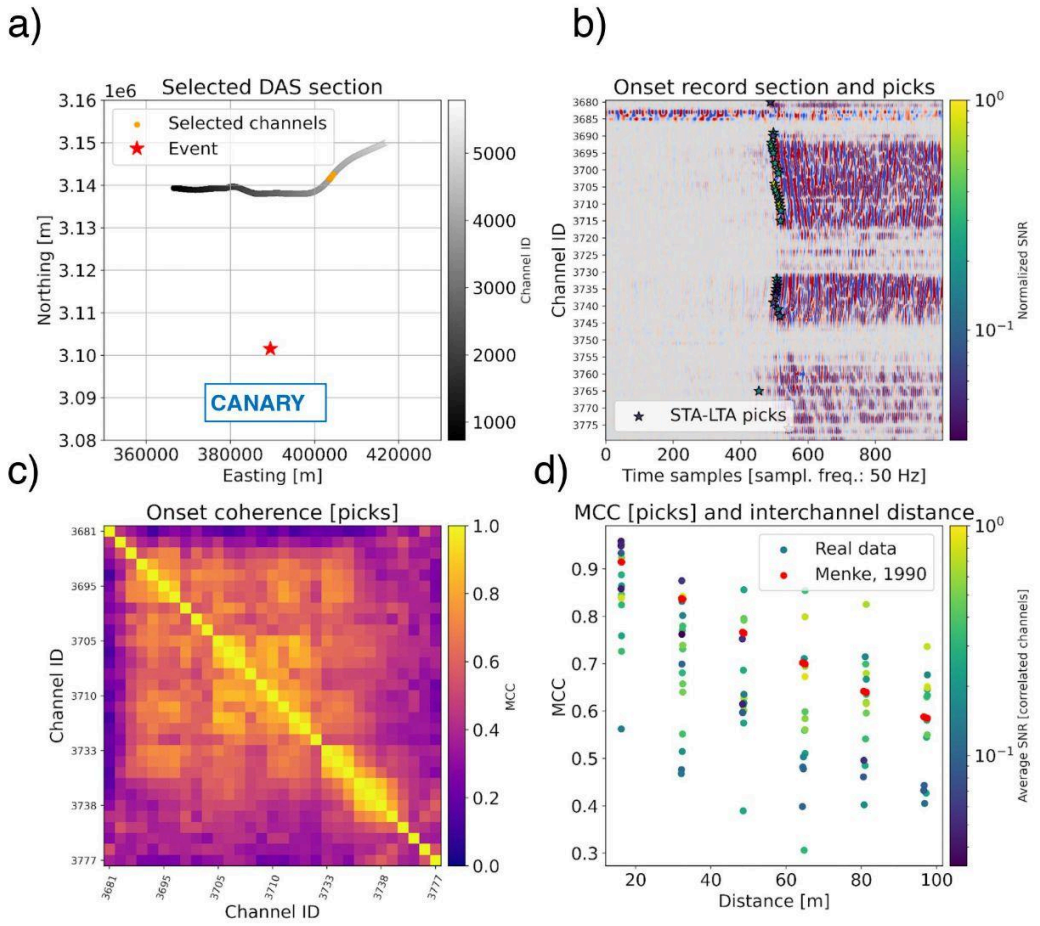

Figure 7. Waveform Correlation Analysis: CANARY case study. a) Selected rectilinear portion; b) Onset record section and triggered channels associated with SNRs (STA-LTA picks as colored stars); c) MCCi matrix for the picked channels; d) MCCi against interchannel distance, limited to 100 m. The average SNRs for the cross-correlated channels are shown with a scale of colors. A theoretical decay, following Menke et al., 1990, is provided as red dots.

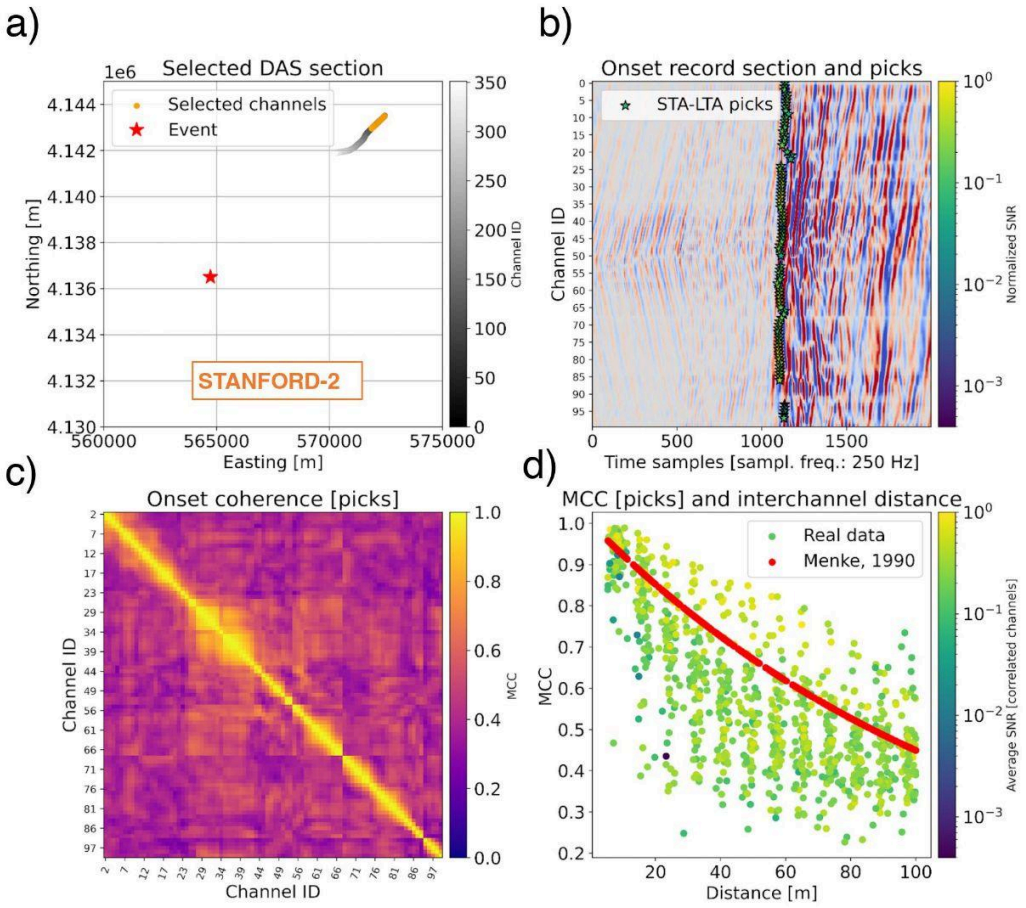

Figure 8. Waveform Correlation Analysis: STANFORD-2 case study. a) Selected rectilinear portion; b) Onset record section and triggered channels associated with SNRs (STA-LTA picks as colored stars); c) MCCi matrix for the picked channels; d) MCCi against interchannel distance, limited to 100 m. The average SNRs for the cross-correlated channels are shown with a scale of colors. A theoretical decay, following Menke et al., 1990, is provided as red dots.

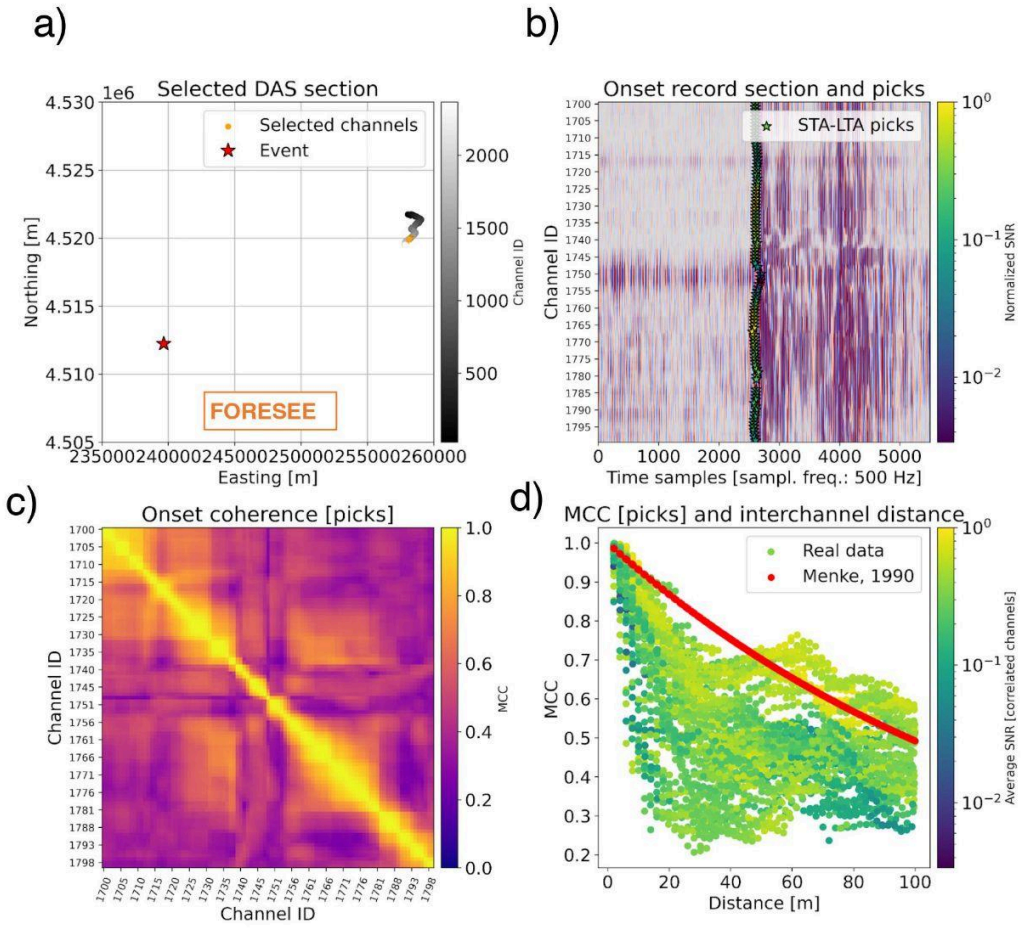

Figure 9. Waveform Correlation Analysis: FORESEE case study. a) Selected rectilinear portion; b) Onset record section and triggered channels associated with SNRs (STA-LTA picks as colored stars); c) MCCi matrix for the picked channels; d) MCCi against interchannel distance, limited to 100 m. The average SNRs for the cross-correlated channels are shown with a scale of colors. A theoretical decay, following Menke et al., 1990, is provided as red dots.

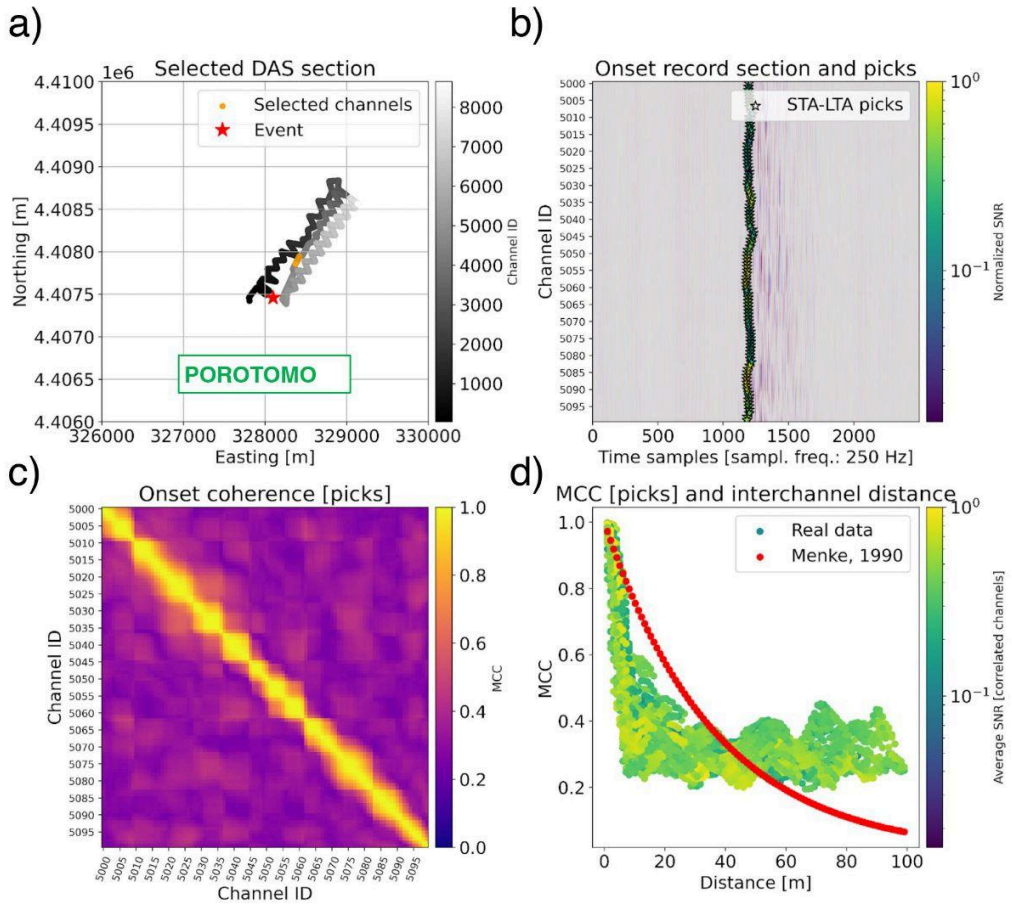

Figure 10. Waveform Correlation Analysis: POROTOMO case study. a) Selected rectilinear portion; b) Onset record section and triggered channels associated with SNRs (STA-LTA picks as colored stars); c) MCCi matrix for the picked channels; d) MCCi against interchannel distance, limited to 100 m. The average SNRs for the cross-correlated channels are shown with a scale of colors. A theoretical decay, following Menke et al., 1990, is provided as red dots.

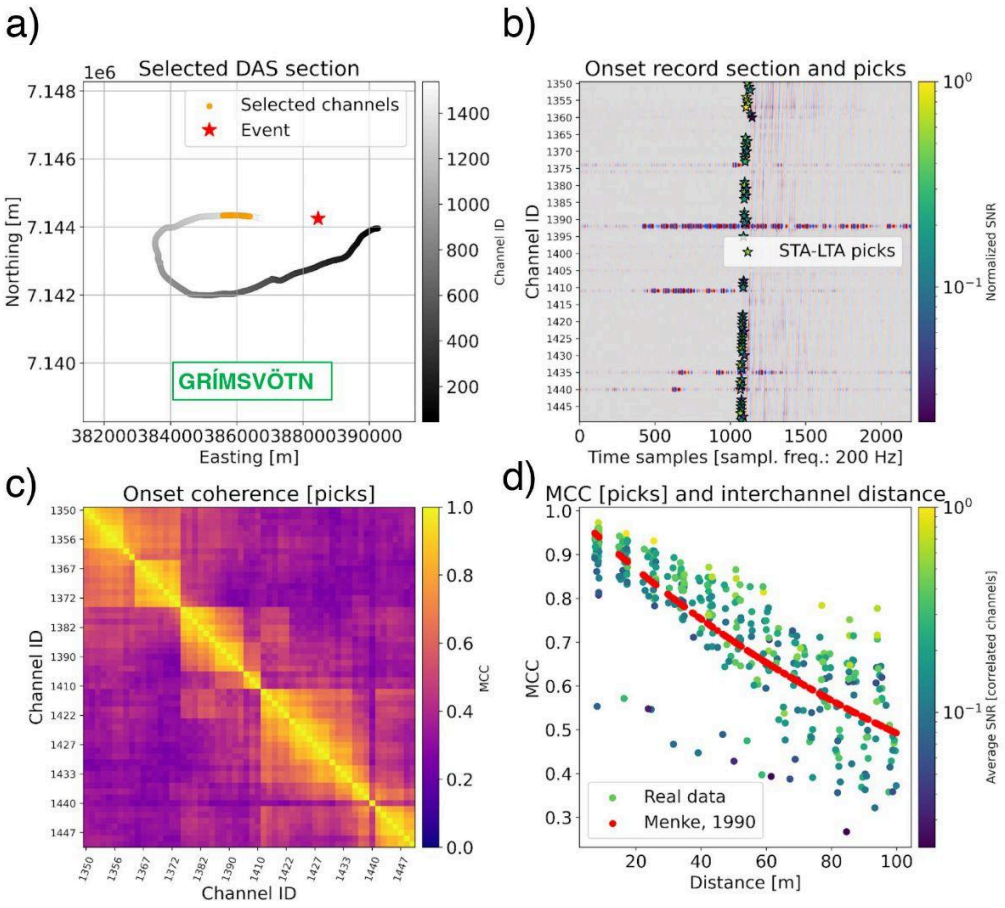

Figure 11. Waveform Correlation Analysis: GRÍMSVÖTN case study. a) Selected rectilinear portion; b) Onset record section and triggered channels associated with SNRs (STA-LTA picks as colored stars); c) MCCi matrix for the picked channels; d) MCCi against interchannel distance, limited to 100 m. The average SNRs for the cross-correlated channels are shown with a scale of colors. A theoretical decay, following Menke et al., 1990, is provided as red dots.

*** manuscript version 11-04-2024 ***